Supplementary Information (SI) for Green Chemistry.

Supplementary Materials for

Radical-driven upcycling of spent graphite into defect-controllable nitrogen-doped graphene for sustainable energy storage

Xiangfei Zeng[a], Yunhui Han[a], Huimin Yang[a], Hao Li[a], Anlong Han[a], Qian Liang[a], Ling Hu[a], Rong Wang[b], Mengjun Chen[a,*]

a. Key Laboratory of Solid Waste Treatment and Resource Recycle (SWUST), Ministry of Education, Southwest University of Science and Technology, 59 Qinglong Road, Mianyang, 621010, China

b. College of National Defense Technology, Southwest University of Science and Technology, Mianyang, 621010

*Corresponding author. E-mail address: kyling@swust.edu.cn (M. Chen).

Table of Contents

1. Material and methods

1.1. Materials

The spent lithium-ion battery graphite (SG) used in this study were obtained from alkali-washed waste graphite supplied by a lithium-ion battery manufacturer in China. The samples were dried at 60 °C and sieved through a 200-mesh screen prior to use. Deionized water was produced using a UPT-11-20TN purification system. Sulfuric acid (98%), phosphoric acid (85%), nitric acid (70%), hydrochloric acid (37%), and potassium hydroxide (KOH), ethanol (EtOH), urea, and N-methyl-2-pyrrolidone (NMP) were purchased from Chengdu Kelong Chemical Reagent Co., Ltd. and used without further purification. Nafion solution (5 wt%) was supplied by DuPont (USA).

1.2. Instruments of characterization.

Characterization of Graphene Samples: X-ray diffraction (XRD) patterns were recorded on a Rigaku Ultima IV diffractometer. Raman spectra were obtained using a Horiba LabRAM HR Evolution spectrometer (Japan) equipped with a 532 nm excitation laser to characterize the structural features of the graphene samples. The spatial resolution of the Raman mapping was determined by a 532 nm laser and a × 50 SLWD VIS objective lens, and the tested wavenumber range was 1100-2300 cm^{-1}. The scanning area was 10 μm × 10 μm with a step size of 1.5 μm. The spatial distribution of defects in the graphene materials was characterized using a TESCAN-WITec RISE correlative SEM–Raman system. Scanning electron microscopy (SEM, Zeiss Sigma 300, Germany) was employed to examine the surface morphology. Convergent-beam electron diffraction (CBED), selected-area electron diffraction (SAED), transmission electron microscopy (TEM), and high-resolution TEM (HRTEM) analyses were conducted using a JEOL JEM-F200 microscope (Japan). Atomic force microscopy (AFM, Bruker Dimension Icon, Germany) was used to determine the thickness and surface topography, with the graphene samples drop-cast onto freshly cleaved mica substrates. The chemical states of the graphite and graphene samples were analyzed by X-ray photoelectron spectroscopy (XPS, Thermo Scientific K-Alpha, USA). Elemental analysis of the materials was performed using an organic elemental analyzer (Elementar Unicube, Germany). Surface roughness of the material was characterized using an optical profilometer (Mahr MarSurf LD130, Germany).

Electrochemical Measurements: The regenerated graphene (8 mg), polyvinylidene fluoride (PVDF) binder, and carbon black conductive agent were mixed in a mass ratio of 8:1:1 in N-methyl-2-pyrrolidone (NMP) and ultrasonically dispersed in a water bath for 30 min. The resulting slurry was uniformly drop-cast onto carbon cloth substrates (1 cm× 1 cm) and dried to obtain flexible electrodes with a final active material loading of approximately 2 mg·cm^{-2}. Electrochemical measurements were conducted in 6 M KOH electrolyte using a platinum foil as the counter electrode and a Hg/HgO electrode as the reference electrode. For oxygen evolution reaction (OER) tests, 10 mg of N-doped graphene and 10 μL of 5 wt% Nafion solution were dispersed in 990 μL of a water/ethanol mixture (1:1, v/v) by ultrasonication for 1 h to form a homogeneous catalyst ink. A 100 μL aliquot of the ink was drop-cast onto acid-treated carbon fiber cloth (1 cm×1 cm) and dried at room temperature, resulting in a catalyst loading of approximately 1 mg·cm^{-2}. A graphite rod and a Hg/HgO electrode were employed as the counter and reference electrodes, respectively, and N_2-saturated 1 M KOH solution was used as the electrolyte. All electrochemical tests were performed on a CHI660E electrochemical workstation (CH Instruments, China). The electrochemical double-layer capacitance (C_{dl}) was derived from the linear fitting of the CV curves collected at different scan rates (10, 20, 30, 40, and 50 mV·s^{-1}) in a non-Faradaic potential region from 0.98 to 1.23 V (vs. RHE). Electrochemical impedance spectroscopy (EIS) measurements were systematically conducted under two specific conditions. For the evaluation of capacitive performance, EIS was recorded at the open-circuit potential (OCP). For the OER kinetics, EIS was performed at the specific applied potential required to deliver a current density of 10 mA·cm^{-2}. All EIS spectra were collected over a frequency range of 100 kHz to 0.01 Hz with an AC voltage amplitude of 5 mV.

Molecular Dynamics Simulation: To investigate the diffusion behavior of $SO_4^{\bullet-}$ in graphitic gallery and $^{\bullet}$OH-modified graphitic gallery systems, a graphite interlayer model with a spacing of 7 Å was constructed based on the stable interlayer spacing of graphite sulfate reported in previous studies[1-3]. To mimic the structure of GO, 35 hydroxyl (–OH) groups were introduced at the edges of the graphene sheets, representing typical oxygen-containing functional groups. Fifty $SO_4^{\bullet-}$ were then randomly inserted into the interlayer region to simulate diffusion under nanoconfined conditions. Intermolecular interactions were described using the OPLS-AA force field, and all simulations were performed using the LAMMPS software package. Initial energy minimization was carried out using the conjugate gradient method to remove any steric clashes or unfavorable configurations. Subsequently, molecular dynamics simulations were performed in the NVT ensemble at 300 K for a total duration of 10 ns to capture both diffusion dynamics and structural evolution. To ensure the reliability and stability of the statistical analysis, mean square displacement (MSD) calculations were based on the trajectories from the final 5 ns of the simulations.

The formula for the Mean Square Displacement (MSD) is given by:

$$MSD(t) = \frac{1}{N}\sum_{i=1}^{N}|r_i(t) - r_i(0)|^2$$

where N is the total number of particles，$r_i(t)$ is the position vector of particle i at time t，$r_0(t)$ s the initial position vector of particle i at time $t = 0$.

The diffusion coefficient is typically calculated based on the Mean Squared Displacement (MSD) of molecules during molecular dynamics simulations, using Einstein's diffusion equation:

$$D = \frac{1}{2d}\lim_{t\to\infty}\frac{d}{dt}\langle|r(t) - r(0)|^2\rangle$$

where the term in braces is the ensemble average of the MSD of the compound.

Density functional theory (DFT) calculations: All DFT calculations were performed using the Vienna Ab initio Simulation Package (VASP)[4, 5]. The generalized gradient approximation (GGA) with the Perdew-Burke-Ernzerhof (PBE)[6] functional was employed to describe exchange–correlation effects. The projected augmented wave (PAW) method[7, 8] was used to represent the interaction between ionic cores and valence electrons, with a plane-wave cutoff energy of 450 eV. Partial occupancies of the Kohn–Sham orbitals were treated using Gaussian smearing with a width of 0.05 eV. The Brillouin zone was sampled using a 1×1×1 Γ-centered k-point grid[9], and all structures were fully relaxed until the total energy converged within 10^{-5} eV and the residual force on each atom was less than 0.02 $eV\cdot Å^{-1}$. A vacuum layer of 17 Å was introduced along the surface normal to eliminate spurious interactions between periodic images. Long-range van der Waals interactions were corrected using the DFT-D3 method with Grimme's empirical scheme[10,11]. Spin polarization was included to account for magnetic effects. The adsorption energy was calculated as:

$$E_{ads} = E_{@adsorbate} - E_{@} - E_{adsorbate}$$

where $E_{@adsorbate}$, $E_{@}$, and $E_{adsorbate}$ are the total energies of the adsorbed system, the clean surface, and the isolated adsorbate molecule, respectively.

The binding energy is defined as $E_{bind}=E_{*adsorbate}-E_{*}-E_{adsorbate}$, where $E_{*adsorbate}$ represents the system single-point energy of the surface with the adsorbate, E_{*} is the single-point energy of a clean surface, and $E_{adsorbate}$ is the single-point energy of the adsorbate molecule.

Life cycle assessment: To evaluate the environmental impacts associated with the synthesis of N-doped graphene from spent graphite (SG) via suspension electrolysis coupled with either hydrothermal or thermal-annealing doping, a life cycle assessment (LCA) was conducted. The assessment employed the ReCiPe 2016 Midpoint (H) V1.07/World (2010) H method, covering 18 environmental impact categories. Quantification and analysis of energy consumption and environmental impacts were performed using SimaPro 9.4 software in combination with data from the Ecoinvent 3 database. Detailed information on the system boundaries, data sources, and calculation parameters is provided in the Section 4 of the Supporting Information.

Normalizing the maximum value of each indicator

The 18 indicators considered in this assessment include: global warming (GW, kg CO_2 eq.), stratospheric ozone depletion (SOD, kg CFC-11 eq.), ionizing radiation (IR, kBq Co-60 eq.), ozone formation (human health) (OF-HH, kg NO_x eq.), fine particulate matter formation (PMF, kg $PM_{2.5}$ eq.), ozone formation (terrestrial ecosystems) (OF-TE, kg NO_x eq.), terrestrial acidification (TA, kg SO_2 eq.), freshwater eutrophication (FE, kg P eq.), marine eutrophication (ME, kg N eq.), terrestrial ecotoxicity (TE, kg 1,4-DCB), freshwater ecotoxicity (FE, kg 1,4-DCB), marine ecotoxicity (MET, kg 1,4-DCB), human carcinogenic toxicity (HCT, kg 1,4-DCB), human non-carcinogenic toxicity (HNCT, kg 1,4-DCB), land use (LU, $m^2\cdot a$ crop eq.), mineral resource scarcity (MRS, kg Cu eq.), fossil resource scarcity (FRS, kg oil eq.), and water consumption (WC, m^3). These indicators were selected to provide a comprehensive analysis of the life cycle impacts of the process.

1.3. Experimental Section

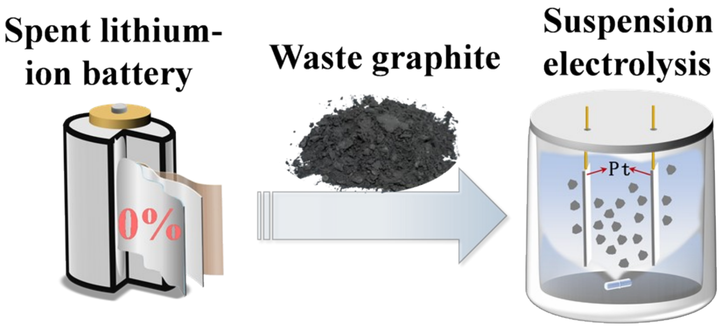

Figure S1. Schematic illustration of the RDWC mechanism triggered by suspension electrolysis.

Suspension electrolytic exfoliation of graphite: In this process, graphite particles are uniformly dispersed in the electrolyte as non-electrode species, establishing a dynamic multiphase reaction interface among the electrode, electrolyte, and graphite particles. Driven by an applied electric field, the RDWC mechanism is triggered within the electrolyte (refer to Section 2 for details), enabling the suspended graphite particles to be exfoliated into graphene in the solution without direct contact with the electrodes.

The experimental setup for the suspension electrolysis of spent graphite (SG) is illustrated in Figure. S1. The electrolytic cell consisted of a 100 mL jacketed beaker equipped with a circulating water cooling system to maintain a constant reaction temperature. High-purity platinum sheets with dimensions of 4cm × 6cm 0.2× mm served as both the anode and the cathode. In a typical procedure, 0.1 g of SG was dispersed in 100 mL of concentrated sulfuric acid electrolyte. Continuous stirring at 300 r/min was applied to establish a homogeneous suspension of graphite particles within the electrolyte. Subsequently, galvanostatic electrolysis was conducted for 5 h. Upon completion of the reaction, the product was collected via filtration, washed, and dried to obtain the regenerated graphene powder.

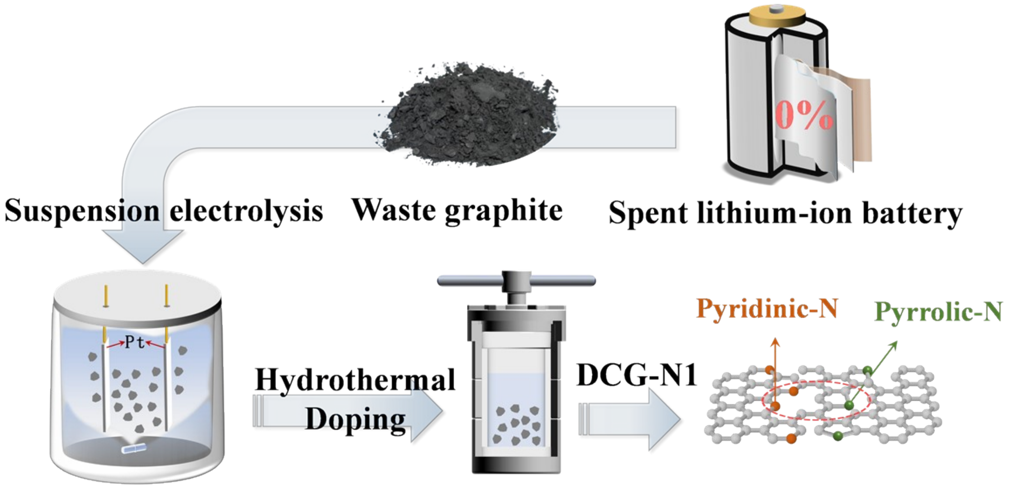

Figure S2. Schematic illustration of the preparation of defect-controllable N-doped graphene (DCG-N1) from SG via the RDWC-based exfoliation-doping route.

Preparation of nitrogen-doped graphene via the RDWC exfoliation-doping route: As shown in Figure. S2, SG was employed as the raw material. The nitrogen-doped graphene precursor was obtained via galvanostatic electrolysis in a sulfuric acid electrolyte at room temperature for 5 h, with a current density of 0.3A/cm^2. Subsequently, the precursor was uniformly mixed with urea at a mass ratio of 1:5 in 50 mL of ultrapure water. The mixture was then subjected to a hydrothermal reaction for 10 h to yield defect-controllable N-doped graphene (DCG-N1). The influence of doping temperature on the nitrogen doping was systematically investigated at 150, 160, 170, and 180°C. To highlight the structural advantages of DCG-N1, a control sample of nitrogen-doped graphene (GO-N) was prepared using commercial graphene oxide as the precursor under identical experimental conditions.

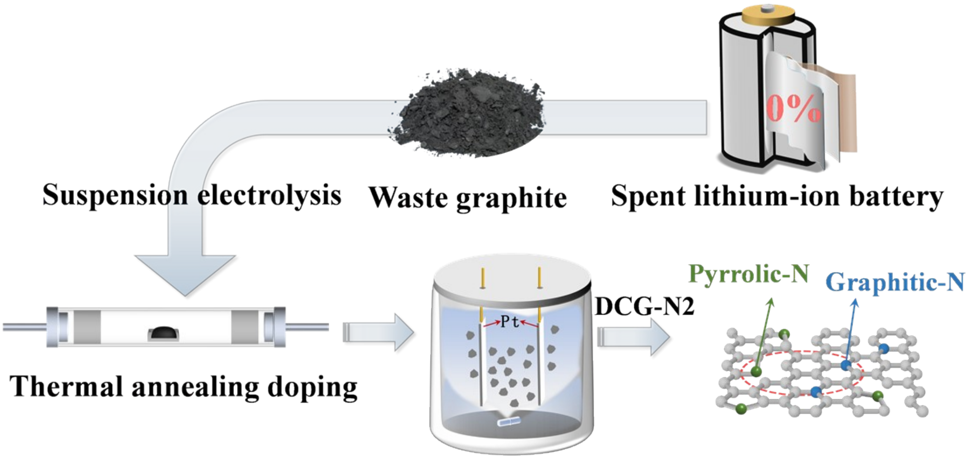

Figure S3. Schematic illustration of the preparation of defect-controllable N-doped graphene (DCG-N2) from SG via the RDWC-based doping-exfoliation route.

Preparation of nitrogen-doped graphene via the RDWC doping-exfoliation route: As shown in Figure. S3, SG was uniformly mixed with urea at a mass ratio of 1:5. The mixture was subjected to a programmed thermal treatment under a nitrogen atmosphere. Specifically, the sample was heated to 550°C at a rate of 5°C min^{-1} and held for 2 h, followed by further heating to 800°C at the same rate with a dwell time of 30 min. The resulting nitrogen-pre-doped graphite powder then underwent suspension electrolysis exfoliation to yield defect-controllable N-doped graphene (DCG-N2). For comparative analysis, a nitrogen-doped sample was also prepared using commercial graphene oxide as the precursor under identical thermal annealing conditions.

Supplementary Text

2. Radical-driven wedge-cleavage (RDWC) mechanism

2.1. Initiating the RDWC process via graphite suspension electrolysis

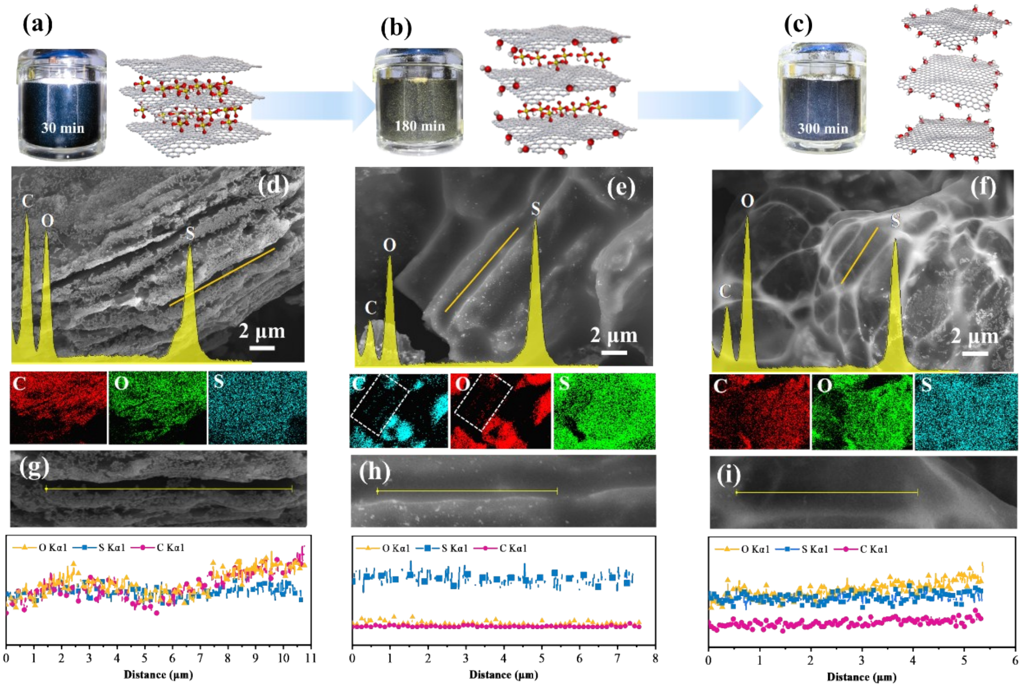

Figure S4. Morphological and structural evolution of spent graphite during suspension electrolysis at key time points: (a–c) Optical photographs and corresponding schematic illustrations of the reaction products at 30 min, 180 min, and 300 min, respectively, (d–f) SEM images at the corresponding time points. The overlaid yellow curves represent the EDS spectra, and the bottom panels display the corresponding EDS elemental mapping images of C, O, and S, (g–i) SEM images of the graphite edges and the corresponding EDS line scan profiles.

Time-dependent SEM analysis was performed at critical intervals (30, 180, and 300 min) during the suspension electrolysis of spent graphite. The evolution clearly delineates three distinct stages: initiation of intercalation, interlayer expansion, and complete exfoliation.In the initial phase (30 min, Figures. S4a, d, and g), SEM imaging (Figure. S4d) reveals a preliminary interlayer expansion of the graphite structure. Both EDS mapping and line scanning indicate a high degree of spatial correlation and signal overlap among C, O, and S elements. This confirms that sulfuric acid molecules, acting as guest species, successfully adsorbed onto the graphite surface and intercalated into the interlayers to form H_2SO_4-GICs[12, 13], thereby inducing the initial expansion of the spent graphite edges.As the reaction proceeded to 180 min (Figures. S4b, e, and h), interlayer expansion became significantly more pronounced (Figure. S4e). EDS mapping shows that C and O are co-distributed within the expanded regions (marked by white frames), whereas S is distributed across the particle surfaces and interlayers. Notably, line scan analysis across the expanded edges reveals a strong overlap between C and O signals, while the S signal exhibits a distinct, independent distribution (Figure. S4h) This suggests that the deep edge expansion at this stage is primarily driven by oxidation reactions involving non-intercalated SO_4^{2-}, where C and O bond at the edges to form hydroxylated graphite species (yellow particles)[14, 15], further facilitating interlayer dilation.By 300 min (Figures. S4c, f, and i), the suspension turned dark gray. As shown in Figure. S4f, the product edges were completely separated, exhibiting a highly curled, semi-transparent, and veil-like morphology characteristic of few-layer graphene. EDS analysis reveals that C and O signals coincide at the thin edges, while S is homogeneously distributed throughout the sample. Line scans in the thin-layer regions further reveal that S and O signals overlap but are spatially separated from the C signal (Figure. S4i); this confirms the completion of interlayer exfoliation, with residual electrolyte adsorbed on the product surface. In summary, the time-dependent SEM analysis unveils that the suspension electrolysis of spent graphite is a controlled, stepwise exfoliation process driven by edge oxidation.

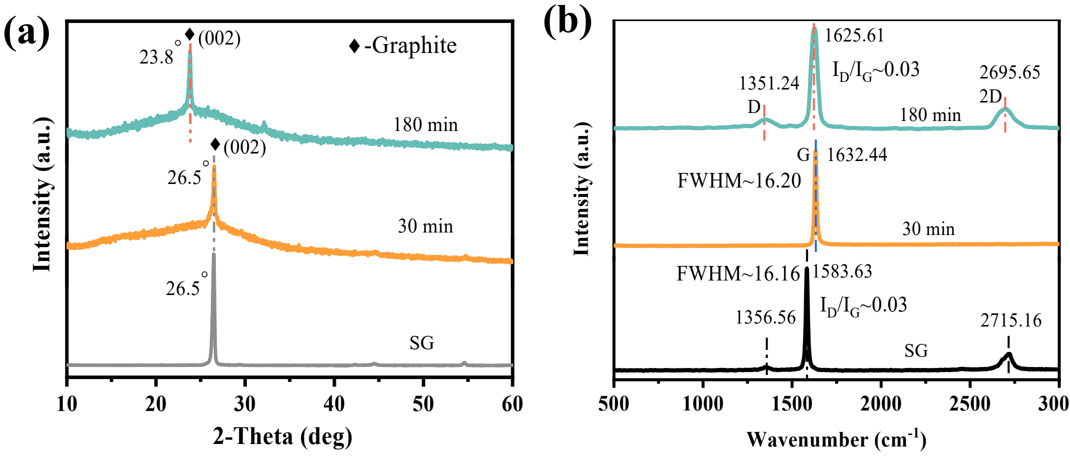

Figure S5. XRD and Raman analyses of products obtained at key time intervals during the suspension electrolysis of SG. (a) XRD patterns of SG and the products obtained after 30 and 180 min of electrolysis, (b) corresponding Raman spectra of SG and the 30, 180 min products.

The dynamic structural evolution of SG during the suspension electrolysis process was investigated using XRD and Raman spectroscopy. The pristine SG displayed a sharp (002) diffraction peak at 26.5°, corresponding to an interlayer spacing of 3.4 Å, indicative of a highly ordered graphitic structure. After 30 min of electrolysis, the (002) peak intensity markedly decreased, reflecting partial disruption of the interlayer stacking. As the electrolysis duration extended to 180 min, the (002) peak further shifted to 23.8°, corresponding to an expanded interlayer spacing of approximately 3.7 Å. This progressive attenuation and leftward shift of the (002) reflection signify continuous intercalation-induced expansion and structural relaxation of the graphite layers, accompanied by a notable decline in crystallographic ordering.

Figure. S5b presents the Raman spectra of the products obtained at different electrolysis durations. After 30 min of electrolysis, a single sharp and intense G band was observed, blue-shifting from 1583.63 to 1632.44 cm^{-1}, with a full width at half maximum (FWHM) of 16.20 cm^{-1}, nearly identical to that of the pristine graphite (16.16 cm^{-1}). This indicates that the sp^2-conjugated carbon framework remained largely intact during the initial stage of suspension electrolysis. The observed blue shift of the G band can be attributed to an increase in the C-C bond force constant induced by local compressive stress and carrier transfer effects. After 180 min of electrolysis, a defect-related D band emerged, accompanied by a slight broadening of the G band. The I_D/I_G ratio remained as low as 0.03, suggesting that only mild exfoliation and limited edge-defect formation occurred, while the overall sp^2 network of graphite was well preserved.

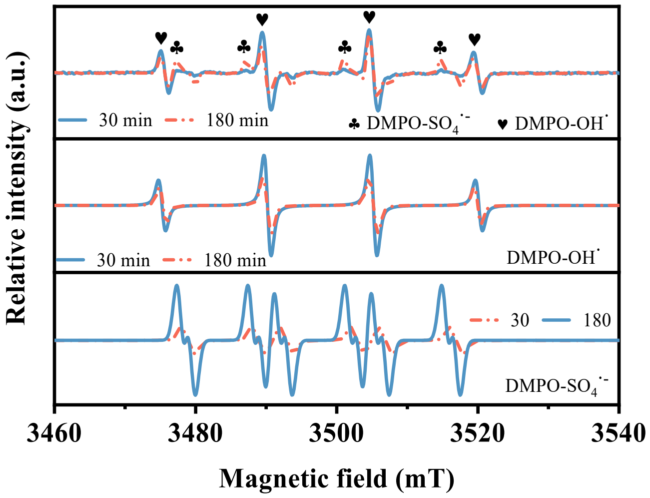

Figure S6. Time evolution of radical relative abundance during the suspension electrolysis process.

At 30 min of electrolysis, the EPR spectra of the electrolyte revealed distinct signals corresponding to $^{\bullet}$OH and $SO_4^{\bullet-}$. The characteristic peak intensity of $^{\bullet}$OH was markedly higher than that of $SO_4^{\bullet -}$, indicating that hydroxyl radicals dominated during the initial stage of the reaction. Owing to their stronger oxidative potential and faster generation kinetics, $^{\bullet}$OH preferentially attacked the edge sites of graphite, inducing mild edge oxidation and localized interlayer stress accumulation. This observation is consistent with the Raman spectrum of the corresponding product, which exhibited a single sharp G band without an apparent D band, confirming that the early stage of electrolysis was primarily governed by $^{\bullet}$OH-driven edge oxidation rather than extensive interlayer disruption or lattice damage.

After 180 min of electrolysis, the intensity of the $^{\bullet}$OH signal significantly decreased, whereas the $SO_4^{\bullet -}$ signal became predominant, indicating a transition in the dominant radical species from $^{\bullet}$OH to $SO_4^{\bullet -}$. The sustained generation of $SO_4^{\bullet -}$ drove the evolution from the $^{\bullet}$OH-mediated edge-oxidation phase to the $SO_4^{\bullet -}$-dominated interlayer insertion and diffusion. Continuous migration of $SO_4^{\bullet -}$ radicals into the graphite galleries facilitated a non-destructive exfoliation process, enabling efficient separation of graphene layers while preserving the integrity of the sp^2-hybridized carbon framework.

2.2. DFT Calculations

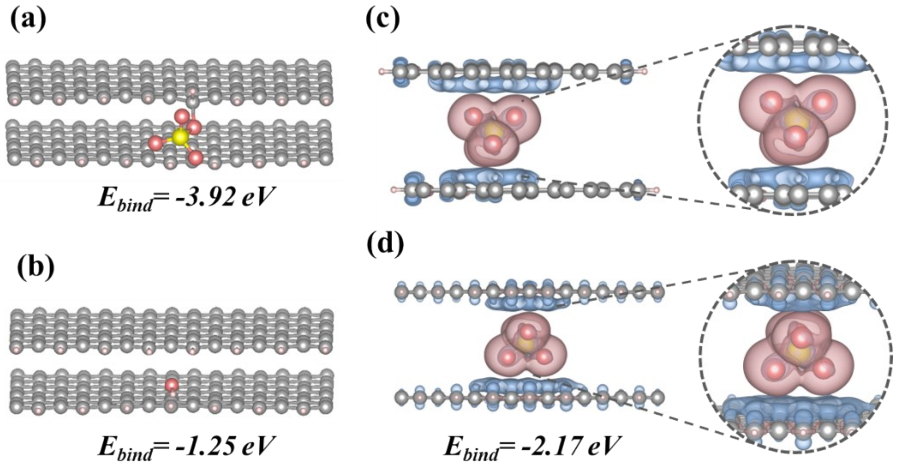

Figure S7. DFT calculations of interactions between radicals and graphite galleries. (a, b) Adsorption energies of $SO_4^{\bullet -}$ and $^{\bullet}$OH at the graphite edge, Charge density difference maps of the intercalated system from the (c) side view and (d) front view, featuring locally magnified insets. The red and blue regions represent charge accumulation and charge depletion.

DFT calculations reveal that the adsorption energies (E_{ads}) of $SO_4^{\bullet -}$ and $^{\bullet}$OH on the edge sites of the graphite (002) plane are -3.92 eV and -1.25 eV, respectively. This result indicates that $SO_4^{\bullet-}$ exhibits a much stronger interaction with the graphite edge, favoring stable adsorption and interlayer insertion. In contrast, the weaker interaction between $^{\bullet}OH$ and graphite suggests that $^{\bullet}OH$ mainly contributes to early-stage edge oxidation and local stress accumulation, thereby creating accessible pathways for the subsequent and sustained intercalation of $SO_4^{\bullet-}$.

The differential charge density analysis further substantiates this mechanism. Pronounced electron accumulation occurs around the intercalated $SO_4^{\bullet-}$ species, while adjacent graphite layers exhibit notable electron depletion. This charge redistribution generates an interfacial dipole and enhances the local electric field, which weakens the interlayer π–π interactions and induces electrostatic repulsion between neighboring layers. These cooperative effects collectively drive the non-destructive exfoliation of graphite. The calculated binding energy of -2.17 eV further confirms that the migration of $SO_4^{\bullet-}$ into the graphite galleries is thermodynamically favorable.

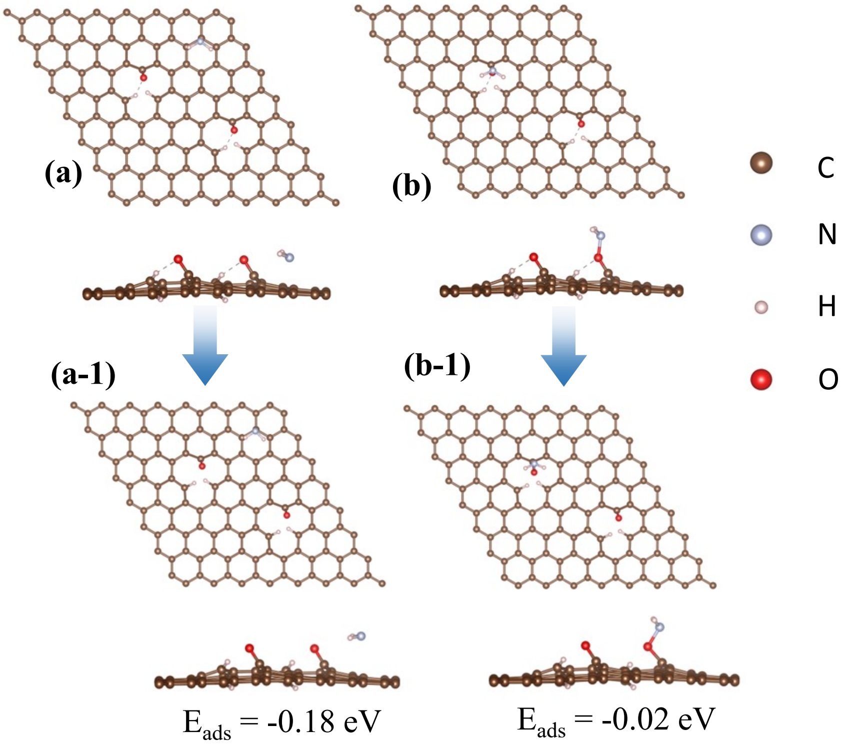

Figure S8. DFT simulation of $–NH_2$ adsorption on the surface of graphene precursor from SG suspension electrolysis. (a, b) Initial adsorption configurations of the amino group ($–NH_2$) at the C site and O site, respectively, (a-1, b-1) The corresponding optimized (relaxed) structures.

In the exfoliation-doping route, DFT calculations reveal that the adsorption of the $–NH_2$ intermediate on the pristine graphene basal plane is highly unstable (E_{ads}=-0.18eV). Due to the lack of local reactivity, the intermediate tends to spontaneously desorb during the structural relaxation process. In contrast, –NH_2 exhibits stable adsorption at the edge oxygen-containing defects introduced by suspension electrolysis (E_{ads}=-0.02). This indicates that edge defects effectively disrupt the intrinsic chemical inertness of the graphene lattice. By enhancing local charge polarization, these defects significantly boost the capture and activation efficiency of nitrogen-source molecules, thereby facilitating efficient edge-nitrogen doping.

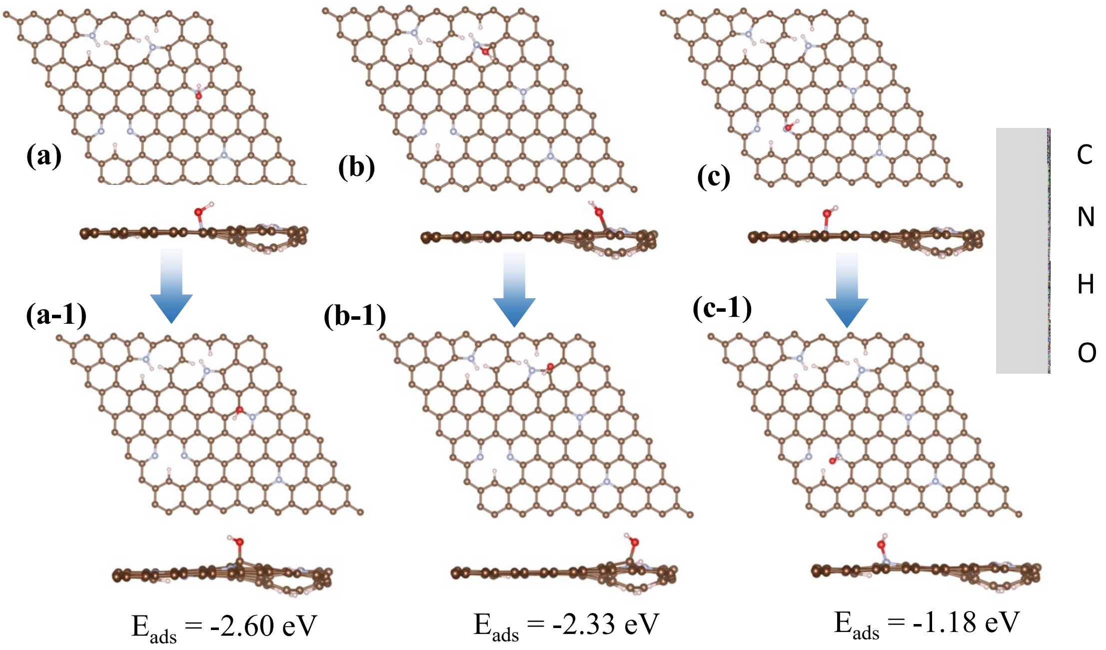

Figure S9. DFT simulation of •OH on nitrogen-doped graphene sites. (a–c) Adsorption configurations of ·OH at Graphitic-N, Pyrrolic-N, and Pyridinic-N sites, respectively. (a-1–c-1) The corresponding optimized (relaxed) structures.

The computational results reveal a pronounced disparity in site selectivity. For both graphitic-N and pyrrolic-N, the •OH spontaneously migrates from the N site to the adjacent C site upon structural relaxation, forming highly stable adsorption configurations with adsorption energies of -2.60 eV and -2.33eV, respectively. This phenomenon indicates that the N atoms in these configurations possess a low intrinsic affinity for •OH. Instead, the surrounding N–C skeleton exhibits high structural robustness, effectively shielding the N site from direct oxidative attack by sacrificing the adjacent carbon atoms, thereby preserving these nitrogen species during the exfoliation process. In contrast, within the pyridinic-N environment, the optimized •OH remains stably adsorbed directly on the N atom, with an adsorption energy of -1.18 eV. This suggests that pyridinic-N possesses significantly higher chemical reactivity, making it highly susceptible to strong interactions with $^{\bullet}$OH, which leads to direct oxidation or substitution.

2.3. RDWC-derived edge-confined defective graphene (DCG) from SG

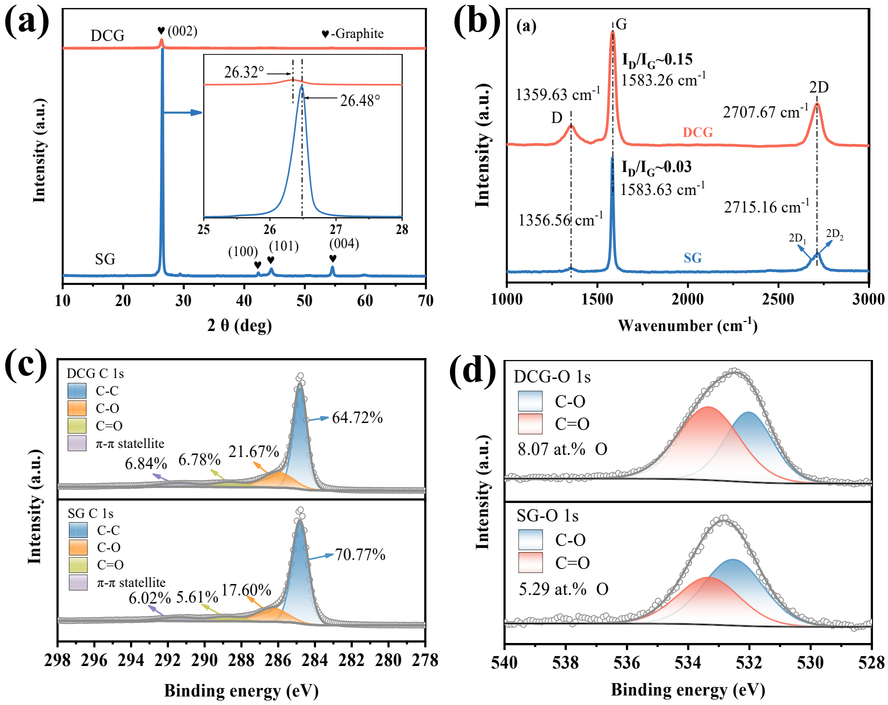

Figure S10. Structural characterization of SG and DCG. (a) XRD patterns, with the inset showing the magnified view of the (002) diffraction peak, (b) Raman spectra, (c) High-resolution C 1s XPS spectra, (d) High-resolution O 1s XPS spectra.

(a–b) Crystal structure analysis: The XRD (002) peak intensity of DCG decreased to 6.09% of the pristine value, accompanied by a shift to 26.32°. This, combined with the disappearance of the 2D peak splitting and its enhanced intensity in the Raman spectrum, confirms the successful exfoliation of graphene. An I_D/I_G ratio of ~0.15 indicates a low defect density in the product.

(c–d) Chemical composition analysis: The O 1s spectrum reveals an increase in oxygen content to 8.07 at.%. The deconvoluted C 1s spectrum shows that the sp^2-carbon content in DCG (64.72%) is only marginally lower than that of spent graphite (70.77%), while the C–O and C=O contents increased to 21.67% and 6.78%, respectively.

These results demonstrate that the RDWC strategy introduces a moderate amount of oxygen-containing functional groups and defect sites while preserving the integrity of the graphene conjugated conductive backbone. This modification effectively breaks the surface chemical inertness, providing thermodynamically active reaction sites for subsequent nitrogen doping.

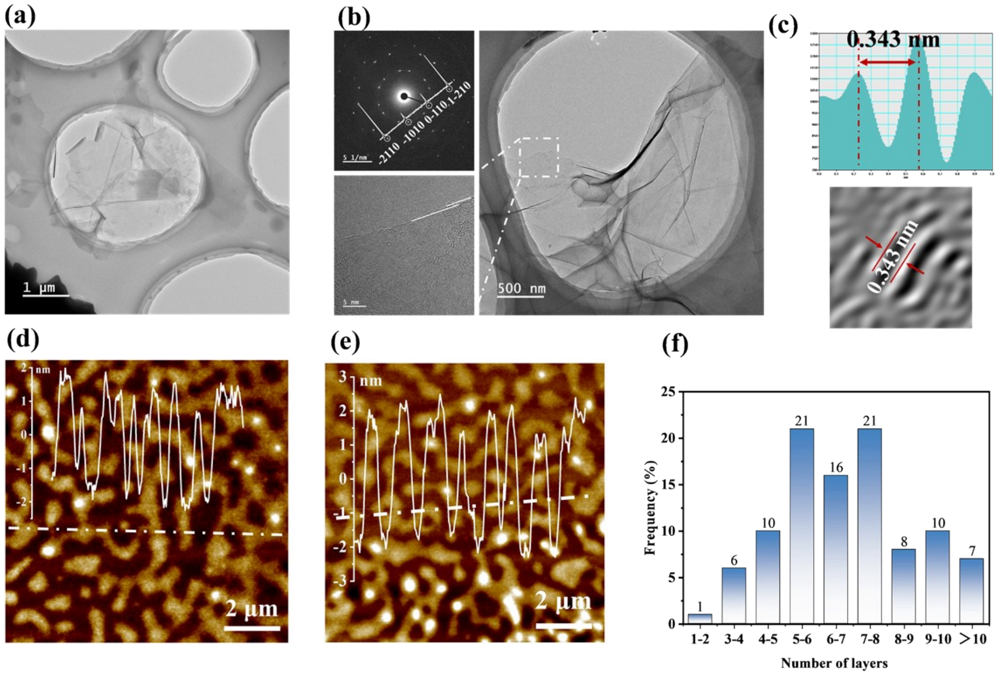

Figure S11. Microscopic morphology and thickness characterization of DCG. (a) TEM image; (b) HRTEM image. The top-left inset shows the corresponding Selected Area Electron Diffraction (SAED) pattern, while the bottom-left inset displays the detailed edge structure; (c) High-resolution HRTEM lattice fringe image and the intensity distribution profile along the red arrow; (d, e) AFM images and the corresponding height profiles along the white dashed lines; (f) Statistical distribution of graphene layer number based on AFM measurements.

(a–c) TEM and SAED analysis: The DCG nanosheets exhibit micron-scale lateral dimensions, with the SAED pattern displaying hexagonal symmetry. The intensity ratio of $I_{1100}/I_{2110} \approx 0.28$ and an interlayer spacing of 0.343 nm confirm the few-layer graphene structure.

(d–f) AFM statistical analysis: A typical nanosheet shows a thickness of approximately 3 nm. Statistical analysis of 100 nanosheets reveals an average lateral size of 1.47 μm. The layer number distribution is concentrated primarily in the 5–8 layer range (58%), followed by 8–10 layers (18%) and 1–5 layers (17%).

Table S1. Bonding state distribution (at. %) from high-resolution C 1s and N 1s XPS of the samples

Sample	sp^2 C-C	Pyridinic-N	Pyrrolic-N	Graphitic-N
SG	70.77	/	/	/
RDWC-Graphene	64.72	/	/	/
DCG-N1	63.81	52.96	47.04	/
DCG-N2	67.60	/	26.73	73.27

The elemental analysis in Table S2 indicates that the average oxygen content of SG is 0.71%; in RDWC-Graphene, the oxygen content only increases slightly to 4.04%. Such a minor degree of oxidation is generally insufficient to cause extensive damage to the material's carbon skeleton (conventional chemical oxidation methods, such as the Hummers', typically result in an oxygen content of 30%-50%, accompanied by significant disruption of the basal plane sp^2 structure[16]).

Table S2. Elemental analysis of the samples

Samples	N (%)	C (%)	H (%)	S (%)	O (%)
SG	0.00	98.15	0.31	0.00	0.73
SG	0.00	98.56	0.27	0.00	0.69
RDWC-Graphene	0.00	94.57	0.33	0.41	4.06
RDWC-Graphene	0.00	94.65	0.38	0.36	4.01
DCG-N1	3.25	94.24	0.85	0.59	1.29
DCG-N1	3.27	94.33	0.75	0.54	1.26
DCG-N2	2.29	94.64	0.59	0.49	1.81
DCG-N2	2.26	94.55	0.60	0.47	1.84

Note: SG represents the raw spent graphite, and RDWC-Graphene denotes the exfoliated graphene precursor.

3. Flexible nitrogen doping enabled by RDWC

3.1. RDWC-based exfoliation-doping route (The sample is denoted as DCG-N1)

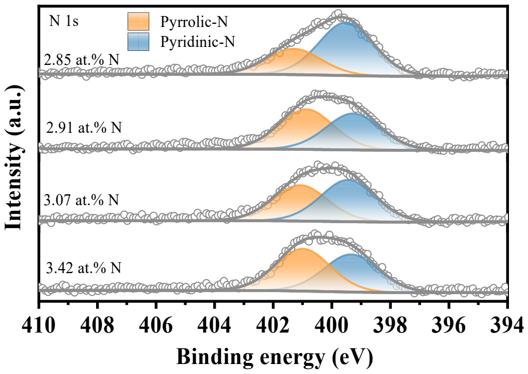

Figure S12. High-resolution N 1s XPS spectrum of DCG-N1. (From top to bottom, the spectra correspond to 150, 160, 170, and 180 °C)

Figure. S12 presents the high-resolution N 1s XPS spectra of hydrothermally N-doped regenerated graphene obtained at different reaction temperatures. As the temperature increased from 150 °C to 180 °C, the nitrogen content rose from 2.85 at% to 3.42 at%, indicating that higher temperatures facilitated the decomposition and activation of urea, thereby enhancing nitrogen incorporation. The deconvoluted N 1s spectra reveal two distinct components centered at ~399.2 eV and ~400.8 eV, corresponding to pyridinic-N and pyrrolic-N species, respectively, confirming that the nitrogen introduced during hydrothermal treatment predominantly exists in these two bonding configurations.

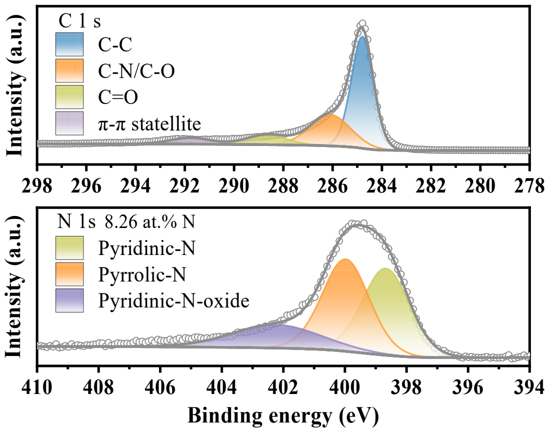

Figure S13. High-resolution C 1s and N 1s XPS spectra of GO-N. (Top) High-resolution C 1s spectrum; (Bottom) High-resolution N 1s spectrum.

The controllable defect-exfoliation mechanism of suspension electrolysis is further validated through comparison with commercial graphene oxide-derived samples

(GO-N). XPS analysis detects oxidized pyridinic-N species in GO-N, in addition to pyridinic- and pyrrolic-N. This is attributed to abundant oxygen functional groups on the GO sp^2-carbon skeleton, which induce side reactions during doping. Since these oxidized species possess significantly lower electrochemical activity, they diminish the overall nitrogen doping efficiency. In contrast, suspension electrolysis offers a distinct advantage: it efficiently converts specific edge defects in DCG into effective nitrogen doping sites, thereby maximizing electrochemical performance.

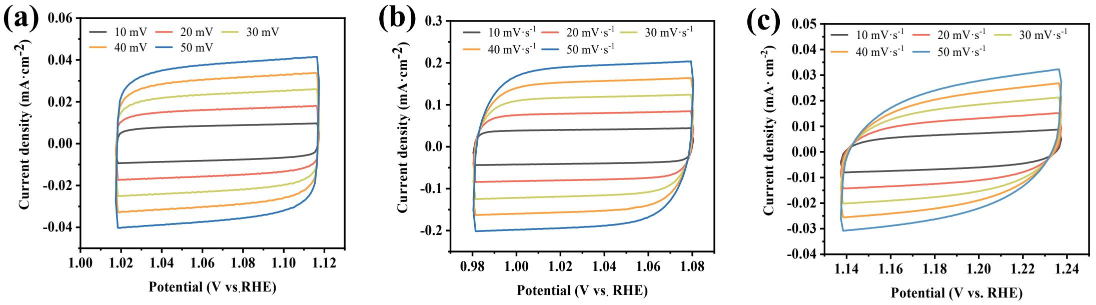

Figure S14. CV curves of DCG-N1_{180} (a), DCG-N1_{170} (b), and GO-N (c) within the non-faradaic region at different scan rates

3.2. RDWC-based doping-exfoliation route (The sample is denoted as DCG-N2)

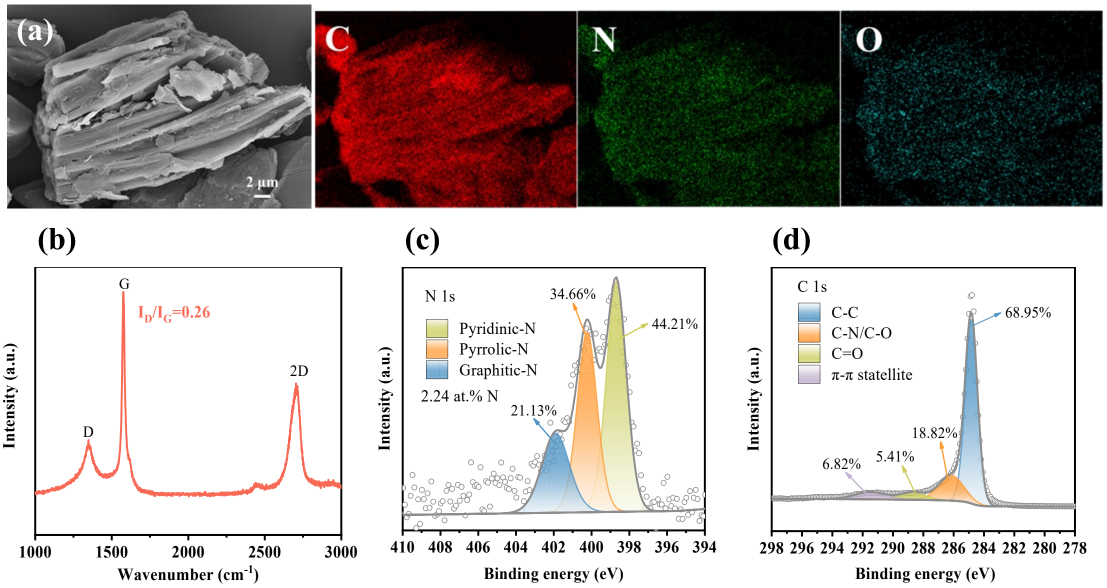

Figure S15. Characterization of the nitrogen-doped graphite (SG-N) precursor prepared from SG via thermal annealing. (a) SEM image, with the corresponding EDS elemental mapping images of C, N, and O displayed on the right; (b) Raman spectrum; (c) High-resolution N 1s XPS spectrum; (d) High-resolution C 1s XPS spectrum.

(a) SEM and EDS analysis: SG-N retains a blocky, layered architecture. The spatial distribution of nitrogen highly overlaps with the carbon framework, indicating uniform bulk doping, while the oxygen signal remains relatively sparse.

(b) Raman spectra: The increase in the I_D/I_G ratio to 0.26 confirms defect generation induced by the incorporation of nitrogen atoms into the lattice.

(c–d) XPS analysis: The N 1s spectrum reveals a total nitrogen content of 2.24 at.%, predominantly composed of pyridinic-N (44.21%) and pyrrolic-N (34.66%). The pronounced π-π satellite peak and the high proportion of C–C bonds (68.95%) in the C 1s spectrum attest to the structural integrity of the carbon backbone.

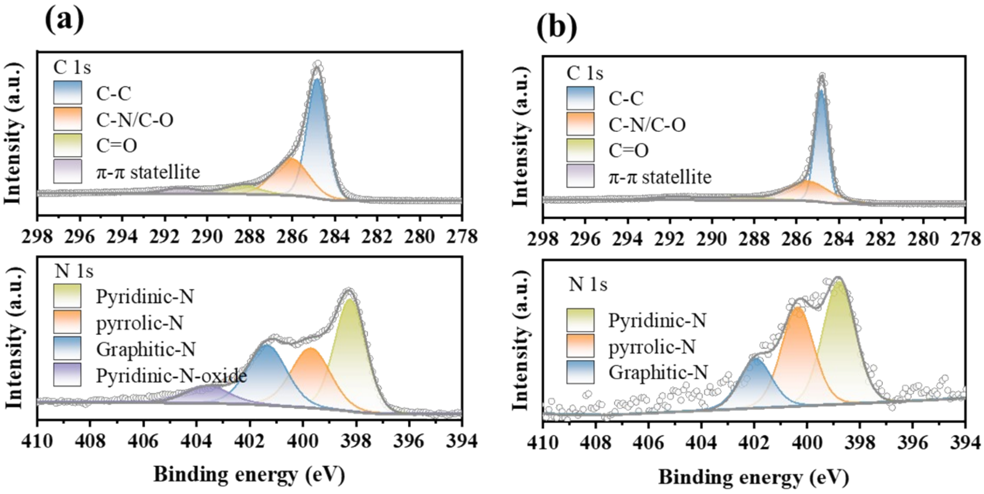

Figure S16. XPS spectra of the nitrogen-doped graphene sample derived from DCG (DCG-T) and the commercial graphene oxide-based nitrogen-doped graphene sample (GO-N1) under identical thermal annealing conditions. (a) High-resolution N 1s (bottom) and C 1s (top) XPS spectra of GO-N1; (b) High-resolution N 1s (bottom) and C 1s (top) XPS spectra of DCG-T.

To elucidate the decisive role of the precursor's intrinsic structure in determining the final doping configuration, we compared the chemical states of DCG-T and GO-N1 under identical thermal annealing conditions.

(a) XPS spectra of the DCG-T: The sample displays intense peaks corresponding to oxygenated carbon species (C–N/C–O and C=O), confirming severe residual oxidation compared to the DCG sample.

(b) XPS spectra of the GO-N1: Due to the extensive oxygen-containing functional groups on the GO scaffold, nitrogen atoms tend to form oxidized pyridinic-N (pyridinic N-oxide) during doping. These inert nitrogen species lower the overall doping efficiency and limit the potential gains in electrochemical activity[17].

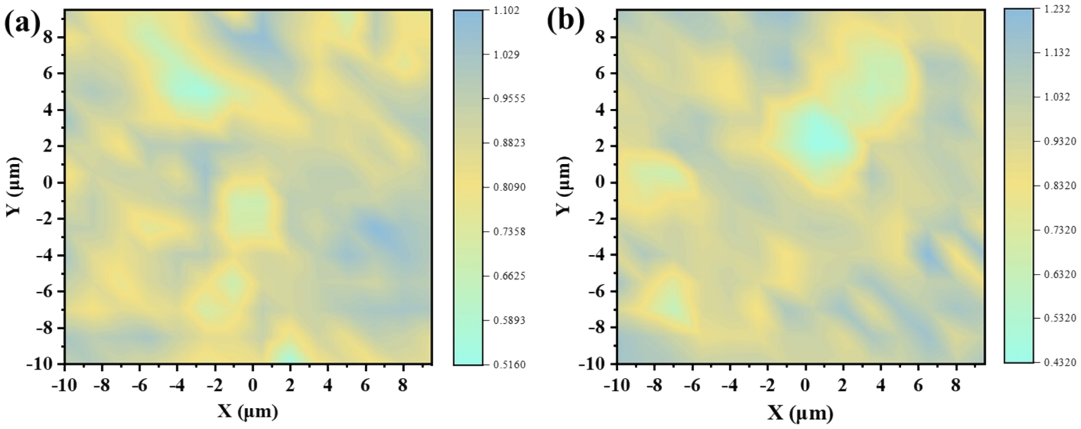

Figure S17. The Raman I_D/I_G mapping results of the (a) DCG-N1 and (b) DCG-N2 nanosheets confirm the distribution characteristic of defect enrichment at the edges.

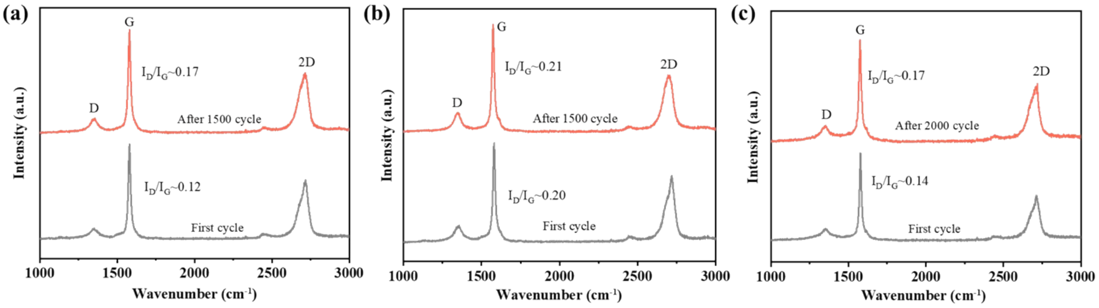

Figure S18. Post-cycling characterizations elucidating the intrinsic origin of the electrochemical stability. (a) DCG-N1 and (b) DCG-N2 electrodes before and after continuous capacitance cycling. (c) Raman spectra of the DCG-N1 electrode before and after extended OER cycling.

Figure. S18 display only a minimal rise in the I_D/I_G values for all electrodes. This demonstrates that prolonged cycling does not inflict structural damage on the carbon basal plane or generate massive defects.

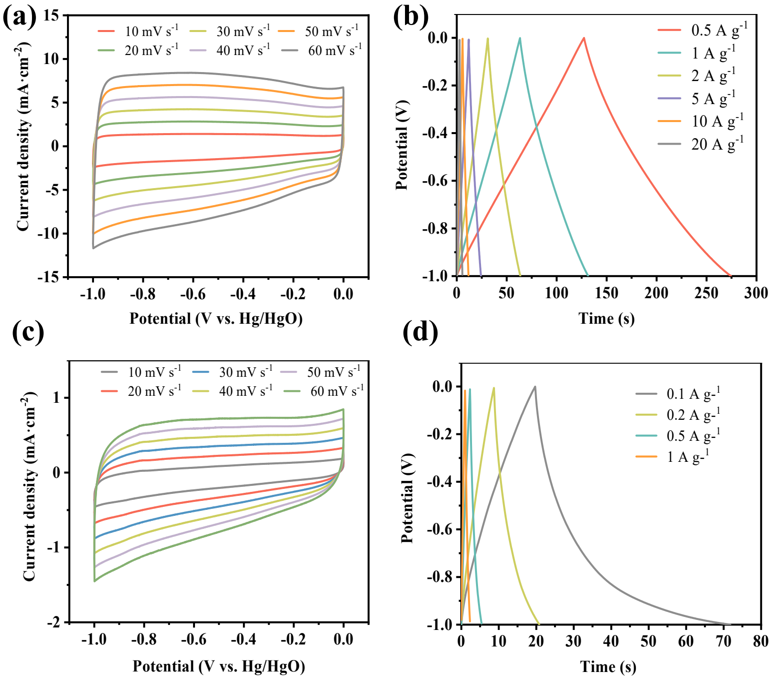

Figure S19. Comparative analysis of capacitive performance for DCG-T and GO-N1. (a, b) CV curves of DCG-T at scan rates from 10 to 60 mV s^{-1}, and GCD curves at current densities from 0.5 to 20 A g^{-1}; (c, d) CV and GCD curves of GO-N1 under similar testing conditions.

(a, b) Electrochemical performance of DCG-T: The sample exhibits a significantly larger CV current response and a near-ideal rectangular profile characteristic of electric double-layer capacitors (EDLCs). The GCD curves retain highly symmetrical isosceles triangular shapes across a wide current density range of 0.5–20 A g^{-1}, demonstrating excellent electrochemical reversibility and superior rate capability.

(c, d) Performance limitations of GO-N1: In sharp contrast, the performance of GO-N1 is severely constrained by the intrinsic structural defects of its GO precursor. The extensive basal plane defects in GO disrupt electron transport pathways and impede ion diffusion. Even after thermal annealing and doping, the severely damaged conjugated conductive network cannot be effectively restored, resulting in inferior capacitive response and poor rate performance.

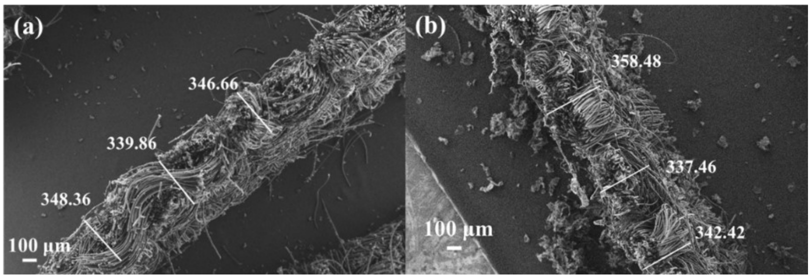

Figure S20. SEM images of the electrode cross-section for OER measurement. (a) DCG-N$_1$170, (b) GO-N

The cross-sectional images (Figures. S20a, b) reveal that DCG-N1$_{170}$ exhibits a thickness of ~344.96 μm, which closely matches the ~346.12 μm thickness observed for GO-N.

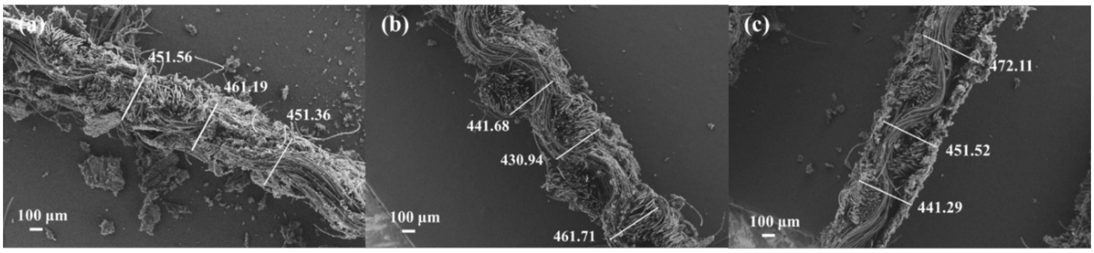

Figure S21. SEM images of electrode cross-sections for capacitance measurement. (a) DCG-N1, (b) DCG-N2, and (c) GO-N

The thicknesses of DCG-N1, DCG-N2, and GO-N were consistently maintained at around 450 μm.

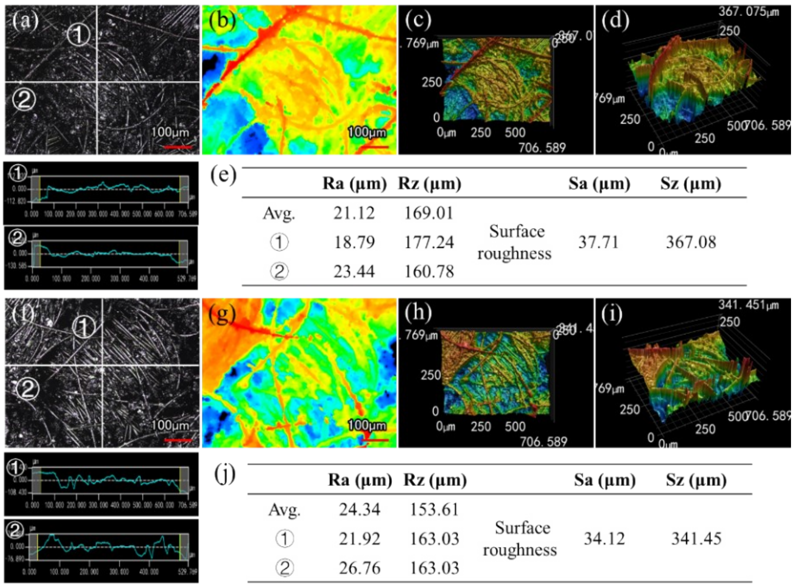

(e)

	Ra (μm)	Rz (μm)		Sa (μm)	Sz (μm)
Avg.	21.12	169.01	Surface roughness	37.71	367.08
①	18.79	177.24			
②	23.44	160.78			

(j)

	Ra (μm)	Rz (μm)		Sa (μm)	Sz (μm)
Avg.	24.34	153.61	Surface roughness	34.12	341.45
①	21.92	163.03			
②	26.76	163.03			

Figure S22. Surface topography and roughness analysis of the fabricated electrodes. (a–e) Morphological and roughness characterizations for the DCG-N$_1$170 electrode, and (f–j) for the GO-N electrode. (a, f) Optical microscopy images and the corresponding cross-sectional line roughness extracted from the selected line scans (labeled as ① and ②). (b, g) False-color 2D height contour maps. (c, d) and (h, i) 3D surface topographical maps of the hierarchical surface architecture. (e, j) Summarized tables presenting the detailed line roughness parameters (Ra, Rz) and areal surface roughness parameters (Sa, Sz) obtained from the profilometry measurements.

Optical profilometry further confirms that the two samples have similar surface roughness. The average line roughness (Ra) of DCG-N1$_{170}$ is 21.12 μm (Figures. S22a–e), while that of GO-N is 24.34 μm (Figures. S22f–j). The corresponding areal roughness (Sa) values are 37.71 μm and 34.12 μm, respectively, indicating comparable surface roughness for the two samples.

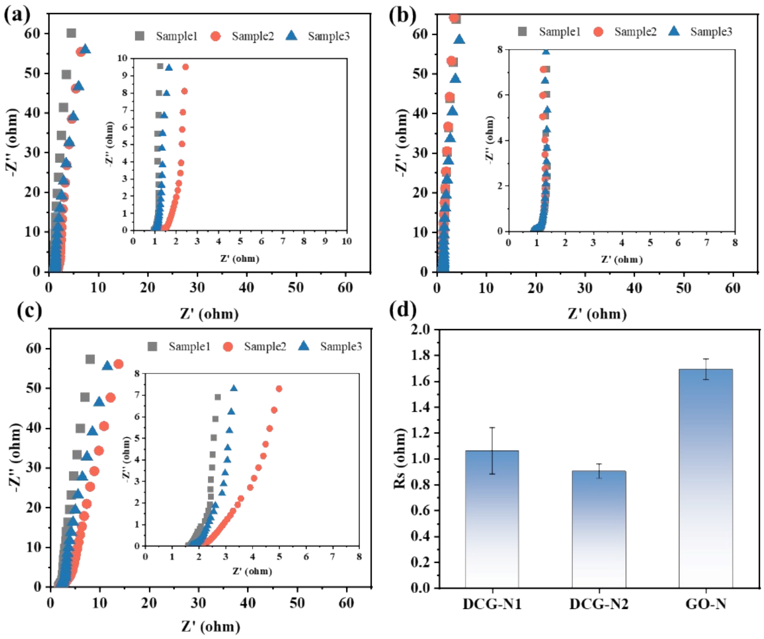

Figure S23. Nyquist plots and Rs values of different samples in capacitive tests. (a) DCG-N1, (b) DCG-N2, and (c) GO-N. (d) Statistical analysis of Rs

The corresponding Nyquist plots and statistical analyses are presented in Figure. S23. Specifically, the statistical results for the Rs are as follows: 1.06±0.17 Ω for DCG-N1, 0.91±0.05 Ω for DCG-N2, and 1.69±0.08 Ω for GO-N. The magnitude sequence of the Rs values is DCG-N2 < DCG-N1 < GO-N.

4. Life cycle assessment

4.1. LCA of the RDWC-based exfoliation-doping route

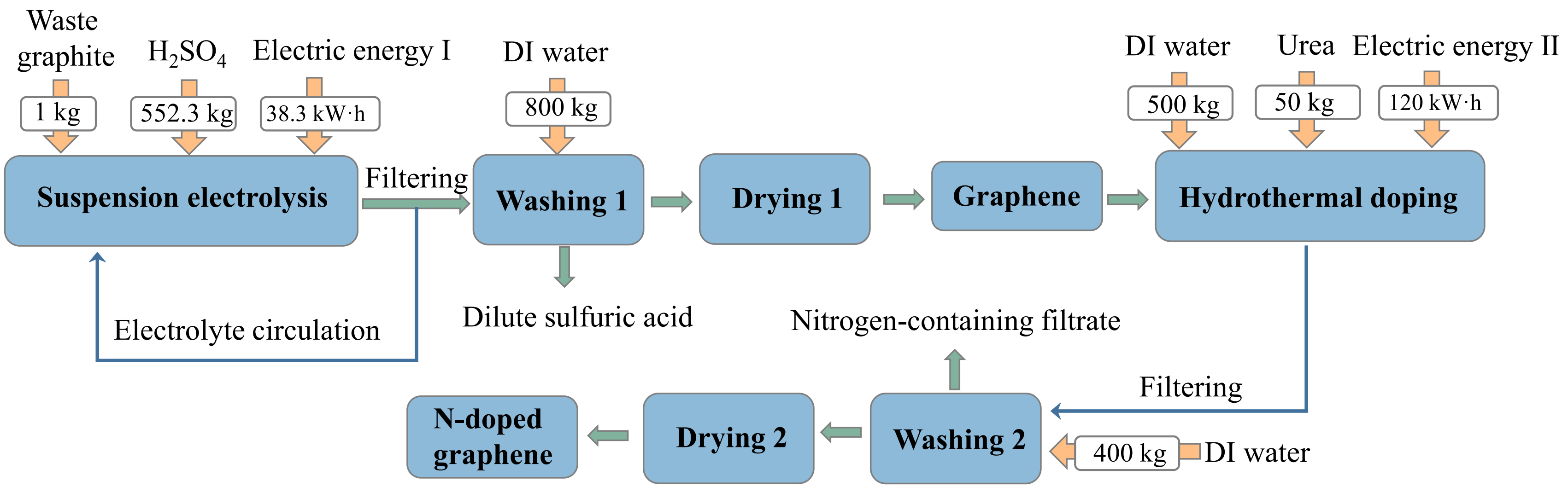

Figure S24. System boundary diagram for the preparation of nitrogen-doped graphene from SG via the RDWC exfoliation-doping pathway.

Material and energy inputs for producing 1 kg of N-doped graphene from SG via suspension electrolysis and hydrothermal treatment: 552.3 kg H_2SO_4, 50 kg of urea, 38.3 kW·h (electrolysis), 20.37 kW·h (post-processing, including stirring, filtration, and drying), and 120 kW·h (hydrothermal doping). Wastewater from washing was recycled; its energy consumption was excluded from the assessment.

Table S3. Life cycle inventory for producing 1.0 kg of N-doped graphene from SG via the RDWC exfoliation-doping pathway.

Input/ Output	Amount	Unit	Corresponding LCI	Database	Comment
Waste graphite	1	kg	Graphite {GLO}| market for | APOS, U	Ecoinvent 3	Avoided product/ Co-product
Sulfuric acid	552.3	kg	Sulfuric acid {RoW}| market for sulfuric acid | APOS, U	Ecoinvent 3	30% Avoided product/ Co-product
Electricity I (electrolysis& post-processing)	58.67	kW·h	Electricity, low voltage {CN}| market group for | APOS, U	Ecoinvent 3	—
Wastewater for washing1	800	kg	Wastewater, average {RoW}| market for wastewater, average | APOS, U	Ecoinvent 3	Avoided product/ Co-product
Urea	50	kg	[sulfonyl]urea-compound {GLO}| market for | APOS, U	Ecoinvent 3	—
Water for hydrothermal	500	kg	Water, deionised {RoW}| market for water, deionised | APOS, U	Ecoinvent 3	—
Electricity II	120	kW·h	Electricity, low voltage {CN}| market group for | APOS, U	Ecoinvent 3	—
Wastewater for washing2	400	Kg	Water, deionised {RoW}| market for water, deionised | APOS, U	Ecoinvent 3	—

Table S4. Data sources of LCA eigenvalues for producing 1 kg of N-doped graphene from SG via the RDWC exfoliation-doping pathway.

Impact category	Unit	Total	Graphite	Sulfuric acid	Water 1 (Washing 1)	Urea	Water 2 (Hydrothermal doping)	Water 3 (Washing 2)	Electricity I (Electrolysis)	Electricity II (Hydrothermal doping)
Global warming (GW)	kg CO_2 eq	461.6937	-0.06904	-292.254	-0.45354	557.8145	0.160316	0.128253	64.48131	131.8861
Stratospheric ozone depletion (SOD)	kg CFC11 eq	0.000819	-3.4E-08	-8.5E-05	-1.1E-06	0.000864	1.51E-07	1.21E-07	1.36E-05	2.78E-05
Ionizing radiation (IR)	kBq Co-60 eq	25.00144	-0.00456	-14.909	-0.0197	36.80781	0.010993	0.008795	1.02029	2.086838
Ozone formation, Human health (OF-HH)	kg NO_x eq	1.066047	-0.00037	-0.66638	-0.00165	1.188993	0.000374	0.000299	0.178892	0.365895
Fine particulate matter formation (FPM)	kg PM2.5 eq	0.659996	-0.00016	-1.04625	-0.00128	1.403531	0.000413	0.00033	0.099628	0.203773
Ozone formation, Terrestrial ecosystems (OF-TE)	kg NO_x eq	1.09256	-0.00038	-0.68147	-0.00167	1.229431	0.000379	0.000303	0.17928	0.366688
Terrestrial acidification (TA)	kg SO_2 eq	1.214348	-0.00035	-3.04818	-0.00315	3.583836	0.000984	0.000787	0.223427	0.456983
Freshwater eutrophication (FE)	kg P eq	0.22246	-2.4E-05	-0.14325	-0.00201	0.329682	8.88E-05	7.1E-05	0.012447	0.025459
Marine eutrophication (ME)	kg N eq	-0.15783	-1.4E-06	-0.36372	-0.0047	0.208221	6.79E-06	5.43E-06	0.000776	0.001586
Terrestrial ecotoxicity (TET)	kg 1,4-DCB	-2172.13	-0.47421	-5220.86	-2.50083	2815.575	2.277028	1.821622	76.19158	155.8376
Freshwater ecotoxicity (FET)	kg 1,4-DCB	-7.63413	-0.00195	-47.6053	-0.03766	32.82484	0.022573	0.018058	2.346321	4.79902
Marine ecotoxicity (MET)	kg 1,4-DCB	-11.5196	-0.00282	-62.3635	-0.05035	41.84142	0.029587	0.02367	2.956129	6.046284
Human carcinogenic toxicity (HCT)	kg 1,4-DCB	18.25818	-0.00456	-21.7556	-0.1537	33.39945	0.019655	0.015724	2.212287	4.524876
Human non-carcinogenic toxicity (HNCT)	kg 1,4-DCB	-151.952	-0.05688	-921.104	-2.43382	663.9753	0.445979	0.356783	35.09127	71.77352
Land use (LU)	m^2a crop eq	6.68986	-0.00282	-8.22727	-0.02374	12.5451	0.004465	0.003572	0.784985	1.605561
Mineral resource scarcity (MRS)	kg Cu eq	-0.83994	-0.00017	-3.23546	-0.00756	2.274354	0.001912	0.00153	0.041195	0.084257
Fossil resource scarcity (FRS)	kg oil eq	134.2804	-0.01944	-79.5869	-0.09871	175.7851	0.040429	0.032344	12.51999	25.60762
Water consumption (WC)	m^3	4.301898	-0.00033	-9.29374	0.715894	11.7533	0.349205	0.279364	0.163596	0.334608

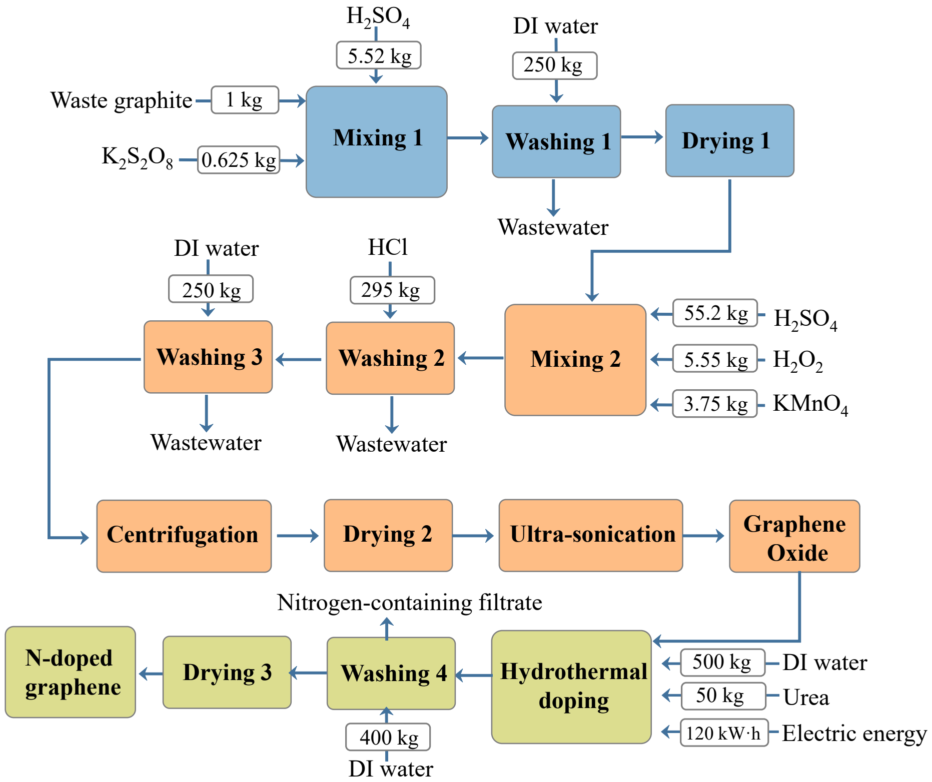

Figure S25. System boundary diagram for the preparation of N-doped graphene from SG via the modified Hummers' exfoliation-doping pathway.

Based on the modified Hummers method for the preparation of graphene oxide, followed by hydrothermal nitrogen doping, the material and energy requirements for producing 1 kg of N-doped graphene from SG were quantitatively evaluated. The system boundary and material inputs were defined according to Lin., et at[18], while the post-processing steps (including stirring, filtration, and drying) were recalculated based on the actual laboratory operations to ensure the accuracy and comparability of the dataset.

Table S5. Life cycle inventory for producing 1.0 kg of N-doped graphene from SG via the modified Hummers' exfoliation-doping pathway.

Input/ Output	Amount	Unit	Corresponding LCI	Database	Comment
Waste graphite	1	kg	Graphite {GLO}| market for | APOS, U	Ecoinvent 3	Avoided product/ Co-product
Electricity	30.57	kW·h	Electricity, low voltage {CN}| market group for | APOS, U	Ecoinvent 3	—
Hydrochloric acid	295	kg	Hydrochloric acid, without water, in 30% solution state {RoW}| market for | APOS, U	Ecoinvent 3	—
Hydrogen peroxide	5.55	kg	Hydrogen peroxide, without water, in 50% solution state {RoW}| market for hydrogen peroxide, without water, in 50% solution state | APOS, U	Ecoinvent 3	—
Potassium permanganate	3.75	kg	Potassium permanganate {GLO}| market for | APOS, U	Ecoinvent 3	—
Potassium sulfate	0.625	kg	Potassium sulfate {RoW}| market for potassium sulfate | APOS, U	Ecoinvent 3	—
Sulfuric acid	60.72	kg	Sulfuric acid {RoW}| market for sulfuric acid | APOS, U	Ecoinvent 3	—
Wastewater for washing 1, 3	500	kg	Wastewater, average {RoW}| market for wastewater, average | APOS, U	Ecoinvent 3	—
Urea	50	kg	[sulfonyl]urea-compound {GLO}| market for | APOS, U	Ecoinvent 3	—
Water for hydrothermal	500	kg	Water, deionised {RoW}| market for water, deionised | APOS, U	Ecoinvent 3	—
Electricity for hydrothermal	120	kW·h	Electricity, low voltage {CN}| market group for | APOS, U	Ecoinvent 3	—
Water for washing 4	400	Kg	Water, deionised {RoW}| market for water, deionised | APOS, U	Ecoinvent 3	—

Table S6. Data sources of LCA eigenvalues for producing 1 kg of N-doped graphene from SG via the modified Hummers' exfoliation-doping pathway.

Impact category	Unit	Total	Graphite	Hydrochloric acid	Hydrogen peroxide	Potassium permanganate	Potassium sulfate	Sulfuric acid	Water 1 (Hydrothermal doping)	Urea	Water 2 (Washing 4)	Water 3 (Washing 1&3)	Electricity I	Electricity II (Hydrothermal doping)
Global warming (GW)	kg CO_2 eq	1017.375	-0.06904	267.7498	8.533801	6.696778	0.665105	9.928197	0.160316	557.8145	0.128253	0.28346	33.59798	131.8861
Stratospheric ozone depletion (SOD)	kg CFC11 eq	0.001119	-3.4E-08	0.000208	2.48E-06	2.75E-06	2.85E-07	6.71E-06	1.51E-07	0.000864	1.21E-07	7.18E-07	7.08E-06	2.78E-05
Ionizing radiation (IR)	kBq Co-60 eq	60.94087	-0.00456	19.80625	0.318027	0.647834	0.028513	0.686441	0.010993	36.80781	0.008795	0.012314	0.531622	2.086838
Ozone formation, Human health (OF-HH)	kg NO_x eq	2.439502	-0.00037	0.689944	0.01717	0.019083	0.00247	0.061408	0.000374	1.188993	0.000299	0.001029	0.093212	0.365895
Fine particulate matter formation (FPM)	kg PM2.5 eq	2.520957	-0.00016	0.691878	0.012985	0.013229	0.002245	0.140022	0.000413	1.403531	0.00033	0.000797	0.051911	0.203773
Ozone formation, Terrestrial ecosystems (OF-TE)	kg NO_x eq	2.491559	-0.00038	0.698449	0.017904	0.01934	0.002508	0.062477	0.000379	1.229431	0.000303	0.001045	0.093414	0.366688
Terrestrial acidification (TA)	kg SO_2 eq	6.064649	-0.00035	1.398708	0.025514	0.026008	0.006093	0.4477	0.000984	3.583836	0.000787	0.001967	0.116416	0.456983
Freshwater eutrophication (FE)	kg P eq	0.536446	-2.4E-05	0.145013	0.005751	0.003134	0.000434	0.019095	8.88E-05	0.329682	7.1E-05	0.001257	0.006486	0.025459
Marine eutrophication (ME)	kg N eq	0.226946	-1.4E-06	0.012497	0.000555	0.000201	1.91E-05	0.000511	6.79E-06	0.208221	5.43E-06	0.00294	0.000404	0.001586
Terrestrial ecotoxicity (TET)	kg 1,4-DCB	7391.285	-0.47421	2730.509	36.72542	37.19045	16.62945	1553.93	2.277028	2815.575	1.821622	1.563016	39.69962	155.8376
Freshwater ecotoxicity (FET)	kg 1,4-DCB	83.00577	-0.00195	29.42516	0.48009	0.398597	0.15603	13.63725	0.022573	32.82484	0.018058	0.023538	1.22255	4.79902
Marine ecotoxicity (MET)	kg 1,4-DCB	107.1548	-0.00282	38.48426	0.641867	0.527	0.204016	17.78776	0.029587	41.84142	0.02367	0.031471	1.540291	6.046284
Human carcinogenic toxicity (HCT)	kg 1,4-DCB	65.52788	-0.00456	21.98032	1.078674	0.484954	0.086682	2.693318	0.019655	33.39945	0.015724	0.096066	1.152712	4.524876
Human non-carcinogenic toxicity (HNCT)	kg 1,4-DCB	1621.574	-0.05688	586.3074	10.83486	8.295136	2.910421	256.9255	0.445979	663.9753	0.356783	1.52114	18.2843	71.77352
Land use (LU)	m^2a crop eq	23.91276	-0.00282	7.99787	0.14367	0.251351	0.036923	0.903206	0.004465	12.5451	0.003572	0.01484	0.409017	1.605561
Mineral resource scarcity (MRS)	kg Cu eq	5.437266	-0.00017	1.99115	0.023638	0.145821	0.011462	0.87712	0.001912	2.274354	0.00153	0.004726	0.021464	0.084257
Fossil resource scarcity (FRS)	kg oil eq	287.8839	-0.01944	71.35661	2.58237	1.841487	0.177766	3.894444	0.040429	175.7851	0.032344	0.061692	6.52354	25.60762
Water consumption (WC)	m^3	19.65481	-0.00033	5.965356	0.417146	0.071302	0.01159	0.835461	0.349205	11.7533	0.279364	-0.44743	0.085241	0.334608

4.2. LCA of the RDWC-based doping-exfoliation route

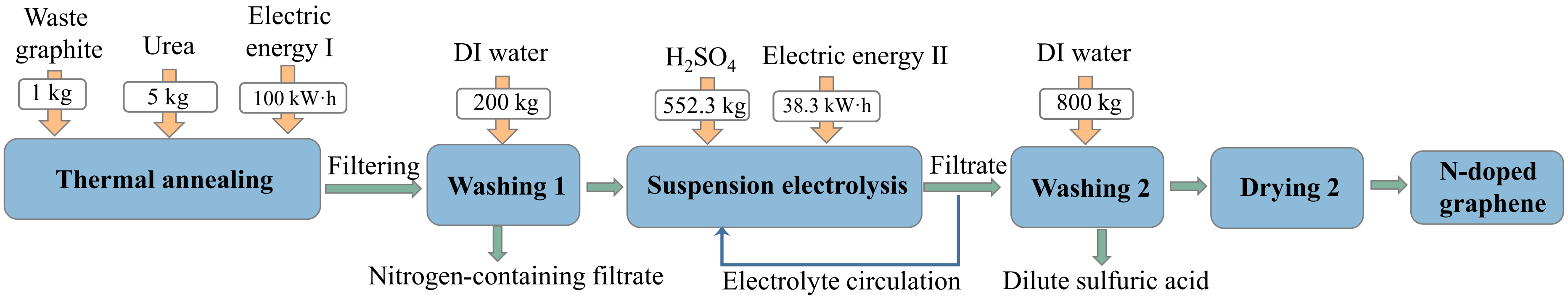

Figure S26. System boundary diagram for the preparation of N-doped graphene from SG via the RDWC doping-exfoliation pathway.

For the production of 1 kg of N-doped graphene from SG via thermal annealing and subsequent suspension electrolysis, the quantified material and energy inputs at the laboratory scale are as follows: 552.3 kg of H_2SO_4, 5 kg of urea, 38.3 kW·h of electricity for electrolysis, and an additional 10.37 kW·h for post-treatment processes including stirring, filtration, and drying. The thermal annealing step consumes approximately 100 kW·h of electricity. The wastewater generated during the washing stage was collected and recycled; the corresponding energy consumption was not included in this assessment.

Table S7. Life cycle inventory for producing 1.0 kg of N-doped graphene from SG via the RDWC doping-exfoliation pathway.

Input/ Output	Amount	Unit	Corresponding LCI	Database	Comment
Waste graphite	1	kg	Graphite {GLO}| market for | APOS, U	Ecoinvent 3	Avoided product/ Co-product
Sulfuric acid	552.3	kg	Sulfuric acid {RoW}| market for sulfuric acid | APOS, U	Ecoinvent 3	30% Avoided product/ Co-product
Electricity II (electrolysis& post-processing)	48.67	kW·h	Electricity, low voltage {CN}| market group for | APOS, U	Ecoinvent 3	—
Wastewater for washing 2	800	kg	Wastewater, average {RoW}| market for wastewater, average | APOS, U	Ecoinvent 3	Avoided product/ Co-product
Urea	5	kg	[sulfonyl]urea-compound {GLO}| market for | APOS, U	Ecoinvent 3	—
Electricity I (thermal annealing)	100	kW·h	Electricity, low voltage {CN}| market group for | APOS, U	Ecoinvent 3	—
Wastewater for washing 1	200	Kg	Water, deionised {RoW}| market for water, deionised | APOS, U	Ecoinvent 3	—

Table S8. Data sources of LCA eigenvalues for producing 1 kg of N-doped graphene from SG via the RDWC doping-exfoliation pathway.

Impact category	Unit	Total	Graphite	Sulfuric acid	Water1 (Washing 2)	Urea	Water2 (Washing 1)	Electricity I (Electrolysis)	Electricity II (Hydrothermal doping)
Global warming (GW)	kg CO$_2$ eq	-73.5353	-0.06904	-292.254	-0.45354	55.78145	0.064126	53.4908	109.9051
Stratospheric ozone depletion (SOD)	kg CFC11 eq	3.48E-05	-3.4E-08	-8.5E-05	-1.1E-06	8.64E-05	6.03E-08	1.13E-05	2.32E-05
Ionizing radiation (IR)	kBq Co-60 eq	-8.66269	-0.00456	-14.909	-0.0197	3.680781	0.004397	0.846387	1.739032
Ozone formation, Human health (OF-HH)	kg NO$_x$ eq	-0.09604	-0.00037	-0.66638	-0.00165	0.118899	0.000149	0.148401	0.304912
Fine particulate matter formation (FPM)	kg PM2.5 eq	-0.6547	-0.00016	-1.04625	-0.00128	0.140353	0.000165	0.082647	0.169811
Ozone formation, Terrestrial ecosystems (OF-TE)	kg NO$_x$ eq	-0.10613	-0.00038	-0.68147	-0.00167	0.122943	0.000152	0.148723	0.305573
Terrestrial acidification (TA)	kg SO$_2$ eq	-2.12673	-0.00035	-3.04818	-0.00315	0.358384	0.000394	0.185345	0.380819
Freshwater eutrophication (FE)	kg P eq	-0.08074	-2.4E-05	-0.14325	-0.00201	0.032968	3.55E-05	0.010326	0.021216
Marine eutrophication (ME)	kg N eq	-0.34564	-1.4E-06	-0.36372	-0.0047	0.020822	2.71E-06	0.000643	0.001322
Terrestrial ecotoxicity (TET)	kg 1,4-DCB	-4748.29	-0.47421	-5220.86	-2.50083	281.5575	0.910811	63.20512	129.8646
Freshwater ecotoxicity (FET)	kg 1,4-DCB	-38.4078	-0.00195	-47.6053	-0.03766	3.282484	0.009029	1.946403	3.999183
Marine ecotoxicity (MET)	kg 1,4-DCB	-50.7299	-0.00282	-62.3635	-0.05035	4.184142	0.011835	2.452272	5.03857
Human carcinogenic toxicity (HCT)	kg 1,4-DCB	-12.9601	-0.00456	-21.7556	-0.1537	3.339945	0.007862	1.835214	3.77073
Human non-carcinogenic toxicity (HNCT)	kg 1,4-DCB	-768.097	-0.05688	-921.104	-2.43382	66.39753	0.178392	29.11014	59.81127
Land use (LU)	m^{2}a crop eq	-5.00838	-0.00282	-8.22727	-0.02374	1.25451	0.001786	0.651189	1.337967
Mineral resource scarcity (MRS)	kg Cu eq	-2.9106	-0.00017	-3.23546	-0.00756	0.227435	0.000765	0.034173	0.070214
Fossil resource scarcity (FRS)	kg oil eq	-30.3847	-0.01944	-79.5869	-0.09871	17.57851	0.016172	10.38602	21.33968
Water consumption (WC)	m^3	-6.84861	-0.00033	-9.29374	0.715894	1.17533	0.139682	0.135712	0.27884

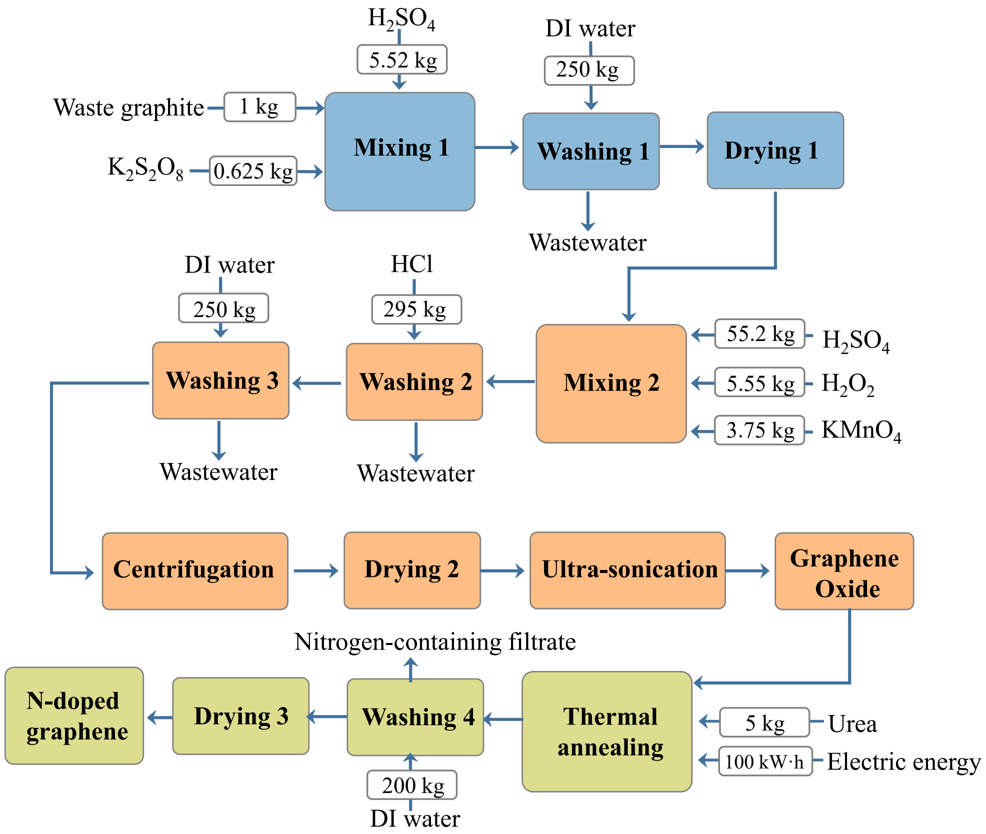

Figure S27. System boundary diagram for the production of N-doped graphene from SG via the modified Hummers' doping-exfoliation pathway.

Based on the modified Hummers method for the preparation of graphene oxide, followed by thermal annealing nitrogen doping, the material and energy requirements for producing 1 kg of N-doped graphene from SG were quantitatively evaluated. The system boundary and material inputs were defined according to Lin., et at [18], while the post-processing steps (including stirring, filtration, and drying) were recalculated based on the actual laboratory operations to ensure the accuracy and comparability of the dataset.

Table S9. Life cycle inventory for producing 1.0 kg of N-doped graphene from SG via the modified Hummers' doping-exfoliation pathway.

Input/ Output	Amount	Unit	Corresponding LCI	Database	Comment
Waste graphite	1	kg	Graphite {GLO}| market for | APOS, U	Ecoinvent 3	Avoided product/ Co-product
Electricity	30.57	kW·h	Electricity, low voltage {CN}| market group for | APOS, U	Ecoinvent 3	–
Hydrochloric acid	295	kg	Hydrochloric acid, without water, in 30% solution state {RoW}| market for | APOS, U	Ecoinvent 3	–
Hydrogen peroxide	5.55	kg	Hydrogen peroxide, without water, in 50% solution state {RoW}| market for hydrogen peroxide, without water, in 50% solution state | APOS, U	Ecoinvent 3	–
Potassium permanganate	3.75	kg	Potassium permanganate {GLO}| market for | APOS, U	Ecoinvent 3	–
Potassium sulfate	0.625	kg	Potassium sulfate {RoW}| market for potassium sulfate | APOS, U	Ecoinvent 3	–
Sulfuric acid	60.72	kg	Sulfuric acid {RoW}| market for sulfuric acid | APOS, U	Ecoinvent 3	–
Wastewater for washing 1, 3	500	kg	Wastewater, average {RoW}| market for wastewater, average | APOS, U	Ecoinvent 3	–
Urea	5	kg	[sulfonyl]urea-compound {GLO}| market for | APOS, U	Ecoinvent 3	–
Electricity for thermal annealing	100	kW·h	Electricity, low voltage {CN}| market group for | APOS, U	Ecoinvent 3	–
Water for washing 4	200	Kg	Water, deionised {RoW}| market for water, deionised | APOS, U		

Table S10. Data sources of LCA eigenvalues for producing 1 kg of N-doped graphene from SG via the modified Hummers' doping-exfoliation pathway.

Impact category	Unit	Total	Graphite	Hydrochloric acid	Hydrogen peroxide	Potassium permanganate	Potassium sulfate	Sulfuric acid	Water, (Washing 4)	Urea	Water 1 (Washing 1&3)	Electricity	Electricity (Thermal annealing)
Global warming (GW)	kg CO_2 eq	493.1367	-0.06904	267.7498	8.533801	6.696778	0.665105	9.928197	0.064126	55.78145	0.28346	33.59798	109.9051
Stratospheric ozone depletion (SOD)	kg CFC11 eq	0.000337	-3.4E-08	0.000208	2.48E-06	2.75E-06	2.85E-07	6.71E-06	6.03E-08	8.64E-05	7.18E-07	7.08E-06	2.32E-05
Ionizing radiation (IR)	kBq Co-60 eq	27.45065	-0.00456	19.80625	0.318027	0.647834	0.028513	0.686441	0.004397	3.680781	0.012314	0.531622	1.739032
Ozone formation, Human health (OF-HH)	kg NO_x eq	1.307904	-0.00037	0.689944	0.01717	0.019083	0.00247	0.061408	0.000149	0.118899	0.001029	0.093212	0.304912
Fine particulate matter formation (FPM)	kg PM2.5 eq	1.223238	-0.00016	0.691878	0.012985	0.013229	0.002245	0.140022	0.000165	0.140353	0.000797	0.051911	0.169811
Ozone formation, Terrestrial ecosystems (OF-TE)	kg NO_x eq	1.323425	-0.00038	0.698449	0.017904	0.01934	0.002508	0.062477	0.000152	0.122943	0.001045	0.093414	0.305573
Terrestrial acidification (TA)	kg SO_2 eq	2.761656	-0.00035	1.398708	0.025514	0.026008	0.006093	0.4477	0.000394	0.358384	0.001967	0.116416	0.380819
Freshwater eutrophication (FE)	kg P eq	0.235365	-2.4E-05	0.145013	0.005751	0.003134	0.000434	0.019095	3.55E-05	0.032968	0.001257	0.006486	0.021216
Marine eutrophication (ME)	kg N eq	0.039273	-1.4E-06	0.012497	0.000555	0.000201	1.91E-05	0.000511	2.71E-06	0.020822	0.00294	0.000404	0.001322
Terrestrial ecotoxicity (TET)	kg 1,4-DCB	4828.107	-0.47421	2730.509	36.72542	37.19045	16.62945	1553.93	0.910811	281.5575	1.563016	39.69962	129.8646
Freshwater ecotoxicity (FET)	kg 1,4-DCB	52.63197	-0.00195	29.42516	0.48009	0.398597	0.15603	13.63725	0.009029	3.282484	0.023538	1.22255	3.999183
Marine ecotoxicity (MET)	kg 1,4-DCB	68.4484	-0.00282	38.48426	0.641867	0.527	0.204016	17.78776	0.011835	4.184142	0.031471	1.540291	5.03857
Human carcinogenic toxicity (HCT)	kg 1,4-DCB	34.68671	-0.00456	21.98032	1.078674	0.484954	0.086682	2.693318	0.007862	3.339945	0.096066	1.152712	3.77073
Human non-carcinogenic toxicity (HNCT)	kg 1,4-DCB	1011.409	-0.05688	586.3074	10.83486	8.295136	2.910421	256.9255	0.178392	66.39753	1.52114	18.2843	59.81127
Land use (LU)	m^2a crop eq	12.34832	-0.00282	7.99787	0.14367	0.251351	0.036923	0.903206	0.001786	1.25451	0.01484	0.409017	1.337967
Mineral resource scarcity (MRS)	kg Cu eq	3.373627	-0.00017	1.99115	0.023638	0.145821	0.011462	0.87712	0.000765	0.227435	0.004726	0.021464	0.070214
Fossil resource scarcity (FRS)	kg oil eq	125.3528	-0.01944	71.35661	2.58237	1.841487	0.177766	3.894444	0.016172	17.57851	0.061692	6.52354	21.33968
Water consumption (WC)	m^3	8.532189	-0.00033	5.965356	0.417146	0.071302	0.01159	0.835461	0.139682	1.17533	-0.44743	0.085241	0.27884

References:

1 S. Seiler, C.E. Halbig, F. Grote, P. Rietsch, F. Börrnert, U. Kaiser, B. Meyer and S. Eigler, Nat. Commun., 2018, 9, 836.

2 A.M. Dimiev, S.M. Bachilo, R. Saito and J.M. Tour, ACS Nano, 2012, 6, 7842-7849.

3 H. Lee, J.I. Choi, J. Park, S.S. Jang and S.W. Lee, Carbon, 2020, 167, 816-825.

4 G. Kresse and J. Furthmüller, Comput. Mater. Sci., 1996, 6, 15-50.

5 G. Kresse and J. Furthmüller, Physical Review. B, Condensed Matter, 1996, 54, 11169-11186.

6 J. Perdew, K. Burke, and M. Ernzerhof, Phys. Rev. Lett. 1996, 77, 3865-3868.

7 G. Kresse and D. Joubert, Phys. Rev. B, 1999, 59, 1758-1775.

8 P. Blöchl,Phys.Rev.B·1994, 50,17953-17979.

9 H. Monkhorst,J.Pack,Phys.Rev.B, 1976, 13(12): 5188.

10 S. Grimme, J. Antony, S. Ehrlich and H. Krieg, J. Chem. Phys., 2010, 132, 154104.

11 S. Grimme, S. Ehrlich and L. Goerigk, J. Comput. Chem., 2011, 32, 1456-1465.

12 N.I. Kovtyukhova, N. Perea-López, M. Terrones and T.E. Mallouk, ACS Nano, 2017, 11, 6746-6754.

13 A.M. Dimiev, G. Ceriotti, N. Behabtu, D. Zakhidov, M. Pasquali, R. Saito and J.M. Tour, ACS Nano, 2013, 7, 2773-2780.

14 J. Guo, S. Pei, K. Huang, Q. Zhang, X. Zhou, J. Tong, Z. Liu, H. Cheng and W. Ren, Nat. Commun., 2025, 16, 727.

15 S. Pei, Q. Wei, K. Huang, H. Cheng and W. Ren, Nat. Commun., 2018, 9, 145.

16 A. Tararan, A. Zobelli, A.M. Benito, W.K. Maser and O. Stéphan, Chem. Mat., 2016, 28, 3741-3748.

17 Y. Zhao, J. Raj, X. Xu, J. Jiang, J. Wu and M. Fan, Small, 2024.21, 2311163.

18 S. Lin, S. Ng and W. Ong, Environ. Pollut., 2021, 288, 117677.